Vicarious Calibration for the AHSI Instrument of Gaofen-5 With Reference to the CRCS Dunhuang Test Site

Kun Tan, *Senior Member, IEEE*, Xue Wang, Chao Niu, Feng Wang, *Member, IEEE*, Peijun Du, *Senior Member, IEEE*, De-Xin Sun, Juan Yuan, and Jing Zhang

***Abstract*— The visible-shortwave infrared Advanced Hyperspectral Imager (AHSI) is a payload onboard the Gaofen-5 satellite, which is China's first hyperspectral satellite and is part of the Chinese High-Resolution Earth Observation System. As a supplement to the onboard radiometric calibration of the AHSI instrument, vicarious calibration is also required, which is independent of the instrument-based calibration. In this article, a reflectance-based vicarious calibration approach is presented, which takes surface reflectance data, aerosol data, and atmospheric water vapor data into account. The Dunhuang test site, which is one of the China Radiometric Calibration Sites (CRCS) for the vicarious calibration of spaceborne sensors, possesses stable, uniform, and measurable surface objects, so it was chosen as the radiation source to replace the laboratory and onboard calibrators. A Spectra Vista Corporation (SVC) spectral radiometer and a CE318 sun photometer were utilized for the measurement of the surface reflectance and the condition of the aerosol, respectively. The radiance at the entrance pupil at the top of atmosphere was then obtained through the MODerate resolution atmospheric TRANsmission (MODTRAN) atmospheric transmission model. The surface reflectance was obtained using the Fast Line-of-sight Atmospheric Analysis of Hypercubes (FLAASH) atmospheric model for validation. The results show that, with regard to the calibration coefficients, the calibrated AHSI instrument presents a stable radiometric performance among different land-cover types. The ratios on all the bands are between 0.8 and 1.2 and are consistent with the reflectance data from the Dunhuang test site. The R^2 values are all greater than 0.95 and the spectral angle is all less than 2°. The standard deviations of the ratios are less than 3% for each chosen band, which proves that the calibrated data have a high consistency with the *in situ* measurements. When compared with Landsat 8 and Sentinel-2, the mean errors of the surface reflectance are all under 0.06, which further demonstrates that the calibrated reflectance has a high accuracy.**

***Index Terms*— Advanced Hyperspectral Imager (AHSI), Gaofen-5 (GF-5), hyperspectral, radiometric calibration, vicarious calibration.**

I. Introduction

With the advent of hyperspectral imagery, which is designed to identify and analyze the physicochemical characteristics of land cover, the importance of absolute radiometric calibration has come to the fore. The Gaofen-5 (GF-5) satellite is an important part of the China High-resolution Earth Observation System (CHEOS). GF-5 carries two optical imaging sensors, along with an atmospheric infrared ultraspectral sounder, a greenhouse gas monitoring instrument, an environmental trace gas monitoring instrument, and a directional polarization camera [1]. The visible-shortwave infrared (SWIR) Advanced Hyperspectral Imager (AHSI), which was designed by the Shanghai Institute of Technical Physics, Chinese Academy of Sciences, Shanghai, China, is one of the main payloads onboard the GF-5 satellite. The AHSI instrument was developed covering 330 spectral bands to characterize the solar reflective regime from 400 to 2500 nm, with a narrow swath width of approximately 60 km. The spectral resolution is about 5 nm for the visible and near-infrared (VNIR) region from 400 to 1000 nm and about 10 nm for the SWIR region from 1000 to 2500 nm. The spatial resolution is around 30 m [2].

To ensure the precision of the radiometric measurements of the AHSI instrument, radiometric calibration is required [3], [4]. Due to the interference of atmospheric transmission, the distortion error of the optical system, variation in the zenith angle and terrain, different observation angles, and the aging of the observation system, there is usually a deviation between the energy observed by the sensor and that truly emitted or reflected by the ground object [5], [6]. In this respect, radiometric calibration helps to eliminate the deviation and allows the data to be used in the field of quantitative research. The objective of radiometric calibration is to acquire the accurate quantitative relationship between the sensor's digital output and the radiance at the sensor's entrance pupil, and to then fix the calibration coefficients [7], [8].

Manuscript received March 6, 2020; revised June 19, 2020; accepted August 2, 2020. Date of publication August 18, 2020; date of current version March 25, 2021. This work was supported in part by the Natural Science Foundation of China under Grant 41871337. *(Corresponding authors: Xue Wang; De-Xin Sun.)*

Kun Tan, Xue Wang, and Chao Niu are with the Key Laboratory of Geographic Information Science (Ministry of Education), East China Normal University, Shanghai 200241, China, and also with the Key Laboratory for Land Environment and Disaster Monitoring of NASG, China University of Mining and Technology, Xuzhou 221116, China (e-mail: wx_cumt@yeah.net).

Feng Wang is with the Key Laboratory for Information Science of Electromagnetic Waves (MoE), Fudan University, Shanghai 200433, China.

Peijun Du is with the Key Laboratory for Satellite Mapping Technology and Applications of NASG, Nanjing University, Nanjing 210023, China.

De-Xin Sun, Juan Yuan, and Jing Zhang are with Qidong Optoelectronic Remote Sensing Center, Shanghai Institute of Technical Physics, Chinese Academy of Sciences, Shanghai 226200, China (e-mail: dxsun@yeah.net).

Color versions of one or more of the figures in this article are available online at https://ieeexplore.ieee.org.

Digital Object Identifier 10.1109/TGRS.2020.3014656

Radiometric calibration is required throughout the life cycle of a hyper-spectrometer and can typically be divided into prelaunch, onboard, and vicarious calibration [9].

Prelaunch calibration [10] in the laboratory is an essential process that determines the central wavelength of each band, the instrument response function, the modulation transfer function, and so on. The results can be regarded as the basis for the assessment of the instrument degradation [11]. It has been proved that the radiance response is affected by both long-term degradation and short-term fluctuation, particularly in the orbital environment during the on-orbit periods [12], which results in huge error if the prelaunch calibration results are still used. For example, it was found that the degradation rates determined for 68 months of observations were 3.5% and 6.0% per year for the NOAA-7 and 9 satellites, respectively [13]. Furthermore, the degradation rates over about 170 days were reported as being 6.6%, 2.4%, and 12.9% in bands 2, 3, and 4, respectively, of the Landsat-4 Thematic Mapper [14]. In this regard, the instrument must be periodically calibrated during the on-orbit period. In order to ensure the quantitative accuracy, different methods can be used to execute on-orbit calibration for the AHSI instrument. Spectral calibration can be carried out by combining the radiometric sampling provided by the onboard LED calibrators and the atmospheric profiles from the polarization observations. Moreover, solar-reflected radiometric calibration can be achieved by applying the onboard Spectralon panel, where the attenuation of the Spectralon panel is monitored by the solar diffuser stability monitor (SDSM). The on-orbit calibration results for the AHSI instrument show that the radiometric error is within 5%.

However, ultraviolet radiation damages the reflective properties of the Spectralon panel, which directly determines the calibration accuracy [15]. Therefore, the uncertainty of the onboard calibration increases as time goes by, so vicarious calibration, which is independent of the instrument-based calibration, must be included as an on-orbit supplement [16]. In this study, vicarious calibration experiments were carried out using reflectance-based methods at the Dunhuang test site in China [17]. We also used a uniform dense grass lawn in Xuzhou, China, for the validation of the calibration results.

The rest of this article is organized as follows. Section II details the vicarious calibration process. Section III describes the data and measurements used in this study. Section IV describes the calibration results and the validation. Finally, the conclusions of this article are drawn in Section V.

II. Vicarious Calibration

Vicarious calibration involves selecting stable, uniform, and measurable surface objects as the radiation source to replace the laboratory or onboard calibrators [18]. This calibration approach involves measuring the reflectance data of homogeneous land surfaces and the atmospheric properties synchronously or quasi-synchronously during the image acquisition. This task is normally done at field sites that are characterized by a high probability of clear skies, low aerosol loading, flat terrain, and uniform and high surface reflectance [19]. The measurements are extrapolated to establish the spectral radiance at the entrance pupil at the top of atmosphere through a radiative transfer model. The calibration coefficients can then be determined by comparing the results with the radiance from the synchronous image of the site.

In 1987, Frouin and Gautier [20] calibrated the NOAA-7, GOES-5, and GOES-6 VISSR/VAE solar channels based on the White Sands Missile Range in New Mexico in USA, which features well-known reflectance properties, and the calibration accuracy was improved by 8%–13% on the considered channels. With respect to the gradual reduction on wavelengths and the oscillatory variations in the mid-infrared region of the Thematic Mapper sensor, Slater *et al.* [21] calibrated the Landsat 5 Thematic Mapper sensor at the White Sands test site over a period of 22 months, during which time the nadir-view reflectance, aerosol optical depth (AOD), atmospheric pressure, temperature, and humidity were measured during the sensor image acquisition. The results showed a 2.8% standard deviation for the six solar reflective bands. This calibration experiment was the first truly vicarious calibration, and it laid the foundation for the future development of on-site calibration.

In situ measurements are used to determine the spectral directional reflectance of the surface and the spectral optical depth components causing scattering in the atmosphere (aerosols and molecules). The *in situ* measurement methods can be divided into three main categories: 1) reflectance-based methods; 2) irradiance-based methods; and 3) radiance-based methods [22]. Reflectance-based methods depend on ground-based measurements, such as surface reflectance, aerosol, atmospheric water vapor, and so on. These measurement data are inputted to a radiative transfer model to obtain the top of atmosphere radiance. Irradiance-based methods are basically the same as the reflectance-based methods, but the main difference is that the parameters of the AOD model are measured in irradiance-based methods, such as the downwelling, global, and diffuse irradiances, while the parameters are calculated by the radiation transfer model in reflectance-based methods [23]. Radiance-based methods are based on the cross-calibration where the calibration of one satellite sensor is transferred to other uncalibrated systems. *In situ* vicarious calibration has developed rapidly since the 1980s, particularly for business applications such as the SPOT satellite. Test sites have been built in many countries, including the aforementioned White Sands Missile Range in New Mexico, Lake Frome in South Australia, El Lencito (Barrio Blanco) and Salar de Arizaro in Argentina, Lunar Lake and Railroad Valley in USA, La Crau in southern France, and Dunhuang in China.

Because of the simple and effective operation, reflectance-based methods are commonly utilized for the radiometric calibration of Hyperion, NOAA-9/10/14, SPOT-4 VGT, Landsat-7 EMT+, GOES-7 VISSR, and the Medium Resolution Spectral Imager (MERSI), with an accuracy of up to 97% [19], [24], [25]. Based on the widespread application and the mentioned advantages, the reflectance-based methods were utilized for the radiometric calibration of AHSI instrument. In the reflectance-based calibration methods, measurement of the surface reflectance, aerosol, and atmospheric water vapor is needed to calculate the radiance at the entrance pupil of the

AHSI instrument, based on the radiative transfer model. After field investigation ahead of the schedule, a uniform part of the site of about 2 km × 2 km was selected for the subsequent experiments. During the half-hour periods before and after the overpass of the GF-5 satellite, we collected the surface reflectance data over the chosen part using the Spectra Vista Corporation (SVC) spectral radiometer and a diffuse white reference panel. Meanwhile, the sun photometer was used for the measurement of the direct solar irradiance. After extracting the digital number of the pixels corresponding to the measured surface and calculating the average, the calibration coefficients of all the bands could be achieved by linear regression between the digital number and the radiance at the entrance pupil at the top of atmosphere.

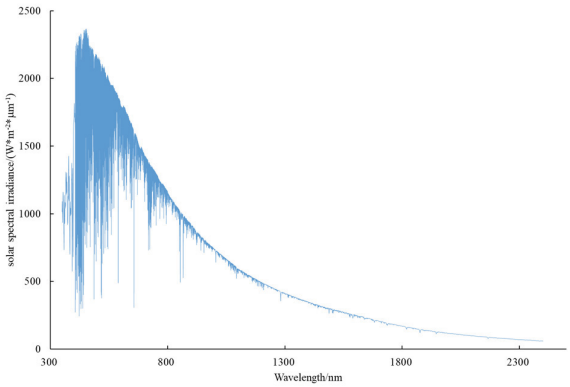

Fig. 1. Solar spectrum curves.

A. Radiative Transfer Model

The MODerate resolution atmospheric TRANsmission (MODTRAN) model was selected as the radiation transmission model in this work, as it can accurately simulate the top of atmosphere radiance by inputting different surface parameters, including atmospheric parameters, sensor parameters, observation geometric parameters, and so on.

The radiance observed by the AHSI instrument is composed of two parts: one part is the energy of the surface radiation reaching the sensor after atmospheric attenuation, and the other part is path radiance, which represents the amount of solar radiation directly backscattered to the sensor by the atmosphere. The mathematical expression of this process is as follows:

$$L = L_p + \frac{\rho_s}{1 - S\rho_s} E_0 \mu_i \gamma_i \gamma_v \tag{1}$$

where L represents the radiance on the entrance pupil of the sensor, L_{P} describes the contribution of the path radiance, and the second term of (1) corresponds to the attenuated energy. ρ_{s} is the surface reflectance measured by the SVC spectral radiometer, S is the spherical albedo of the atmosphere, E_0 denotes the solar radiation flux at the top of atmosphere, μ_i represents the cosine of the incident angle, and γ_i and γ_v are the atmospheric transmittance in the incident direction and the surface to the sensor direction, respectively. Finally, the surface reflectance can be expressed as follows:

$$\rho_s = \frac{L - L_p}{E_0 \mu_i \gamma_i \gamma_v + (L - L_p) S}. \tag{2}$$

If ρ_{s} is set to 0, then L_{P} equals L. After defining $F = E_0 \mu_i \gamma_i \gamma_v$, there are only two unknowns in (2): F and S. The values of S and L can be determined empirically for a certain atmosphere from the MODTRAN model by inputting two different surface reflectance values, such as 0 and 0.5. After this, L can be calculated by substituting the surface reflectance measurement obtained from the ground into (2)

$$L = L_p + \frac{\rho_s F}{1 - \rho_s S}. \tag{3}$$

To account for possible variations in column water vapor across the scene, the solar and satellite angles of the measurement, the aerosol conditions, the temperature, and the water vapor content at the scene are all used in the MODTRAN model; the solar function is from the Kurucz database [26], which is shown in Fig. 1; and the spectral resolution is 1 cm^{-1}.

B. Determination of the Calibration Coefficients

The radiance at the entrance pupil at the top of atmosphere can now be obtained. The next step is to solve the relationship between the digital number of the pixel and the corresponding location radiance, which can be transformed into a gain as follows:

$$\mathrm{Gains} = \frac{L}{\mathrm{DN}} \tag{4}$$

where DN denotes the average digital number of the selected part. The calculation is carried out on each band.

III. Data and Measurements

A. Dunhuang Test Site

The Dunhuang test site is one of the China Radiometric Calibration Sites (CRCS) and was chosen in 1996 as a typical reflectance target for radiometric vicarious calibration. The site is situated between 94.17° E–94.5° E and 40.04° N–40.28° N in the Gobi Desert, as shown in Fig. 2, and is about 15-km West of Dunhuang, Gansu province, China. The observation site is located at the central part of the Danghe alluvial fan, stretching 60 km in the East–West direction and 40 km in the North–South direction. The elevation is approximately 1140 m, the annual precipitation is less than 30 mm, the evapotranspiration is between 2200 to 2400 mm, and the number of cloudless days is 111.3 per year [27]. The surface of the site consists of barren and flat gravel, whose particle size ranges from 0.2 to 0.8 cm [28]. The reflectance of the site is high overall (more than 0.25 after 600 nm), which can ensure that direct solar radiance accounts for the majority of the total radiance. This approach has been proved effective in decreasing the impact of atmospheric scattering during the calculation of the reflectance at the top of atmosphere [22]. On the whole, the geographical and climatic characteristics contribute to the temporal and spatial stability of the spectral features.

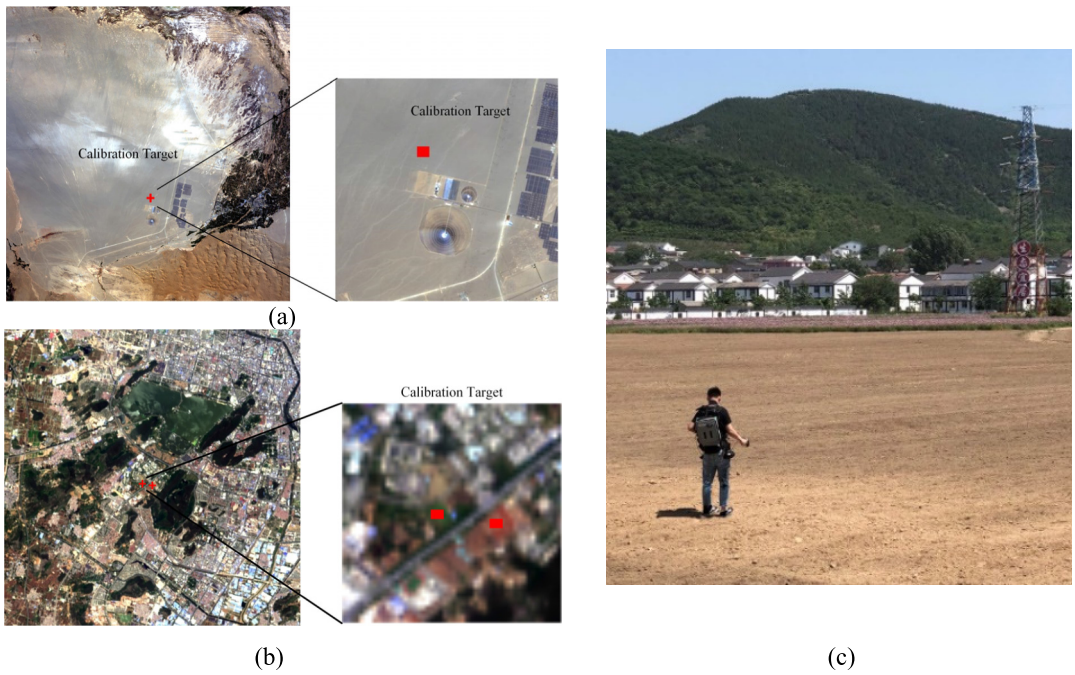

Fig. 2. Geographical location of the calibration target at the test site. (a) Dunhuang test site. (b) Xuzhou test site. (c) Photograph of the ground reflectance collection in Xuzhou.

TABLE I
AHSI DATA USED IN THIS STUDY

	Vicarious calibration data	Validation data		
Location	Dunhuang	Dunhuang		Xuzhou
Data acquisition time (UTC+8)	2019-09-10 14:38:37	2018-09-11 14:50:30	2019-07-14 14:38:42	2019-05-29 13:15:14
Center coordinate	40.1844°N, 94.3740°E	40.2155°N, 94.3079°E	40.1852°N, 94.5968°E	34.2706°N, 117.0094°E
Solar zenith	37.573°	39.081°	21.447°	19.281°
Solar azimuth	204.575°	208.842°	214.349°	233.106°
Satellite zenith	0.077°	6.039°	0.072°	0.071°
Satellite azimuth	158.678°	258.492°	159.514°	158.362°

B. Image Data Acquisition

Four data sets obtained by the AHSI instrument were utilized for the vicarious calibration experiments. One data set was obtained at the Dunhuang test site on September 10, 2019, and was used for the calculation of the calibration coefficients, and the two data sets were acquired at the Dunhuang site on September 11, 2018, and July 14, 2019, and were used for the validation. The other one data set was used to explore the calibration performance among different landcover types which was acquired at the Xuzhou site on May 29, 2019. Further details are provided in Table I.

A cross-validation experiment was also carried out with Landsat 8 and Sentinel-2 images for the validation of the radiometric performance. The details of these near-coincident Landsat 8 and Sentinel-2 scenes are provided in Table II.

C. In Situ Data Acquisition

The CE318 sun photometer and temperature and humidity detectors were utilized to characterize the atmospheric aerosol and water vapor content for the calculation of the radiative transfer model. The CAS Key Laboratory of Infrared System Detection and Imaging Technologies, Shanghai Institute of Technical Physics processed the data. The reflectance at the site surface was measured by an SVC spectral radiometer. As the AHSI instrument was scheduled to acquire an image of the Dunhuang site on September 10, 2019, we collected the spectral data 100 points, with a geographical location of 94.39° E, 40.09° N, as shown in Fig. 2(a) and recorded the synchronous aerosol, water vapor content, temperature, and humidity data, which are listed as follows.

As shown in Fig. 3, the albedo presented a stable trend with little fluctuation around the imaging time, and was, on average, less than 0.25, which can be attributed to the lack of vegetation around the site.

Figs. 3 and 4 show that the AOD and water vapor at the Dunhuang site on September 10, 2019 were of a low amount, indicating that the weather conditions were suitable for vicarious calibration. The error contributed by the

TABLE II
NEAR-COINCIDENT LANDSAT 8 AND SENTINEL-2 DATA USED IN THIS STUDY

Sensor	Location	Data acquisition time (UTC+8)	Center coordinate	Solar zenith	Solar azimuth
Landsat 8	Dunhuang	2018-09-08,12:19:40	40.3278°N, 95.1039°E	41.617°	151.269°
		2019-07-19,12:26:09	40.3280°N, 93.5483°E	25.359°	128.656°
		2019-09-26,12:20:20	40.3267°N, 95.0897°E	42.466°	152.407°
	Xuzhou	2019-06-06,10:42:28	34.6053°N, 118.0839°E	22.179°	119.652°
Sentinel-2	Dunhuang	2018-09-09,12:26:59	40.1455°N, 94.8138°E	37.403°	154.493°
		2019-07-11,12:27:11	40.1455°N, 94.8138°E	23.154°	135.908°
		2019-09-09,12:37:21	40.1455°N, 94.8138°E	37.313°	154.459°
	Xuzhou	2019-06-25,11:08:28	33.8142°N, 117.5213°E	18.235°	131.609°

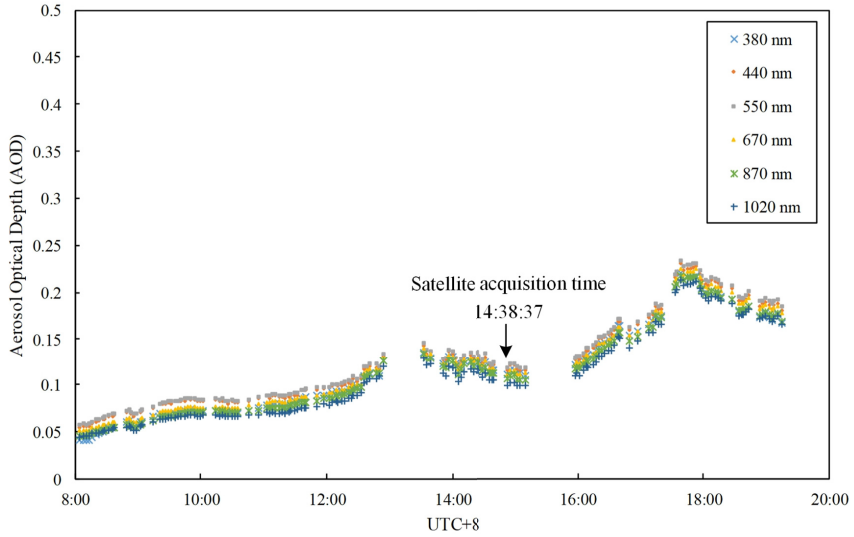

Fig. 3. Diurnal variation of the AOD.

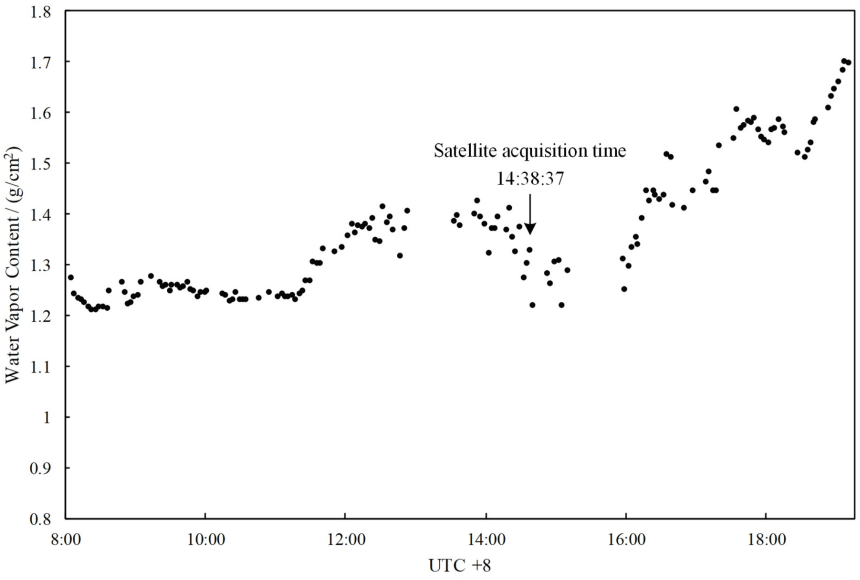

Fig. 4. Diurnal variation of the water vapor content.

atmosphere to satellite measurements is reduced with low values of atmospheric parameters. Moreover, the solar function is from the corrected Kurucz database [26], which is the standard in MODTRAN, and the spectral resolution is 1 cm^{-1}.

IV. RESULTS

A. Calibration Results

After radiometric calibration using the calibration coefficients, the surface reflectance was obtained using the

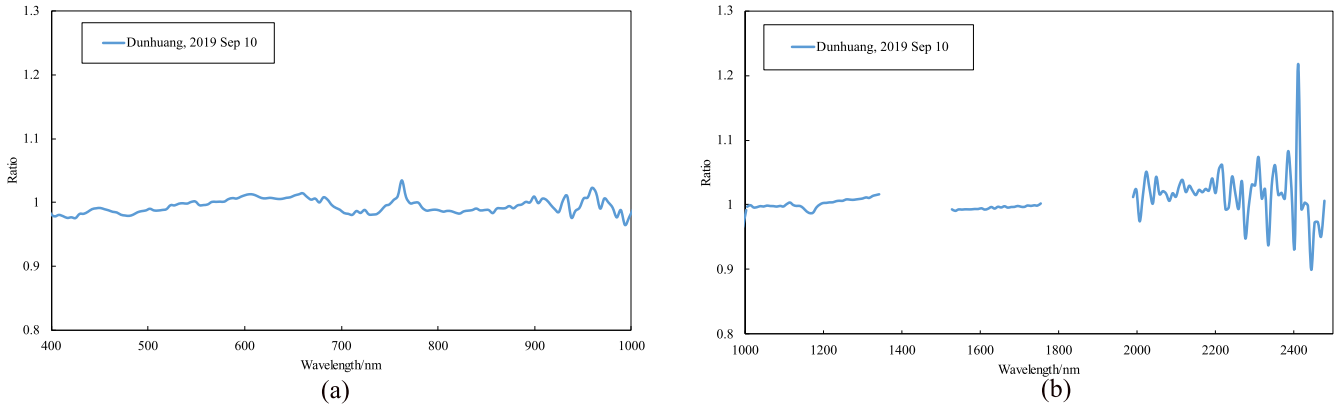

Fig. 5. Ratio of SVC to AHSI surface reflectance for the calibration target from 400 to 2500 nm. (a) VNIR 400–1000 nm. (b) SWIR 1000–2500 nm.

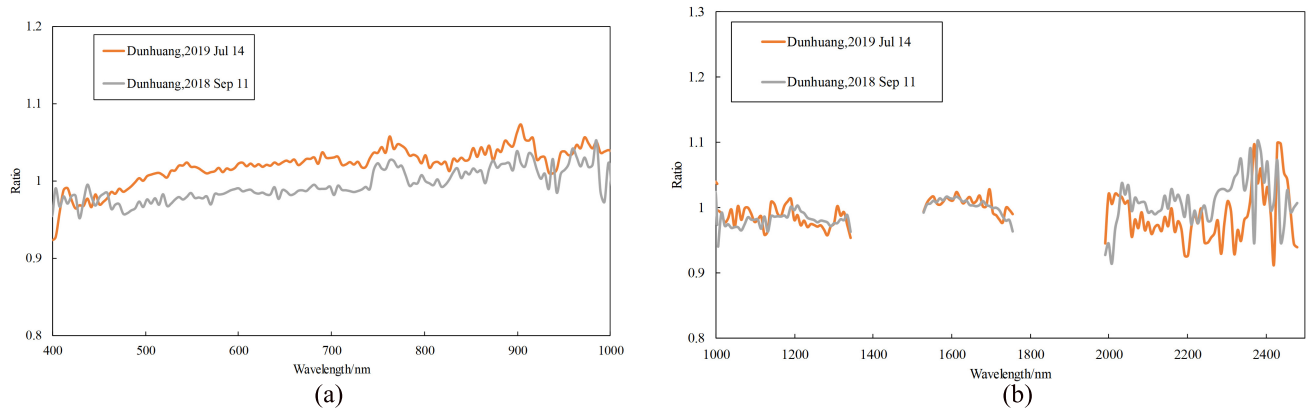

Fig. 6. Ratio of SVC to AHSI surface reflectance on the Dunhuang validation data sets from 400 to 2500 nm. (a) VNIR 400–1000 nm. (b) SWIR 1000–2500 nm.

Fast Line-of-sight Atmospheric Analysis of Hypercubes (FLAASH) atmospheric model. FLAASH is based on MODTRAN4 model, which is one of the basic components of ENVI software and commonly used for atmospheric correction of multispectral and hyperspectral images, and is suitable for objects with flat surface and Lambert reflector properties.

The results are shown as the ratio in the surface reflectance, as determined by the vicarious calibration, compared with the surface reflectance data after removing the water vapor bands. In this case, the surface reflectance data acquired by field spectrometer can be considered to be the true spectra, and the ratio is calculated as follows:

$$\text{Ratio} = \frac{\text{SVC Ref}}{\text{AHSI Surface Ref}}. \tag{5}$$

Fig. 5 shows the ratio of SVC to AHSI surface reflectance for the calibration data set at the Dunhuang site. The calibration spectra for the AHSI instrument show a smaller fluctuation in the VNIR range than the SWIR range at the Dunhuang site. There are obvious peaks near 760 and 940 nm, but the fluctuation is relatively small (about 0.05). It is mainly affected by the water vapor absorption. The ratios of all the bands are between 0.8 and 1.2, and more than 90% of the bands are between 0.95 and 1.05, which are consistent with the SVC measurements. Meanwhile, there is a slight change below 0.2 for the ratio in the SWIR region.

B. Validation Analysis on the Three Data Sets

The selection of appropriate validation data is very important. In order to assess the accuracy of the calibrated spectra, the surface reflectance must be measured on different land-cover categories, such as bare soil and grass. The validation data were collected at the Xuzhou site on May 29, 2018, and the Dunhuang site on September 11, 2018, and July 14, 2019.

Fig. 6 shows the ratios of SVC to AHSI on the two different validation data sets at the Dunhuang site. Most bands have a small fluctuation under ± 0.05, except the bands among 2000 to 2500 nm which mainly caused by the water vapor absorption. The consistency of the reflectance on calibration data sets and validation data sets demonstrates the validation of the calibration coefficients, besides the stability of the AHSI. For a further validation analysis, the R^2 and the spectral angle of the calibration spectra were calculated

$$\text{spectral angle} = \cos^{-1}\left(\frac{x_i^{\mathrm{T}} x_j}{\sqrt{x_j^{\mathrm{T}} x_j}\sqrt{x_i^{\mathrm{T}} x_i}}\right) \tag{6}$$

where x_i and x_j are two reflectance. The smaller the spectral angle is, the more similar the two spectra are. The value

TABLE III
VICARIOUS CALIBRATION RESULTS COMPARED WITH THE SVC MEASUREMENTS AT THE DUNHUANG SITE

Wavelength (nm)	Average reflectance ratio (SVC reflectance/predicted vicarious reflectance)	Standard deviation (%)
467.346	0.9693	1.5296
570.032	0.9860	1.6035
651.31	1.0003	1.2813
800.989	0.9993	1.1135
1611.79	0.9943	2.1185
2201.44	1.0015	2.9375

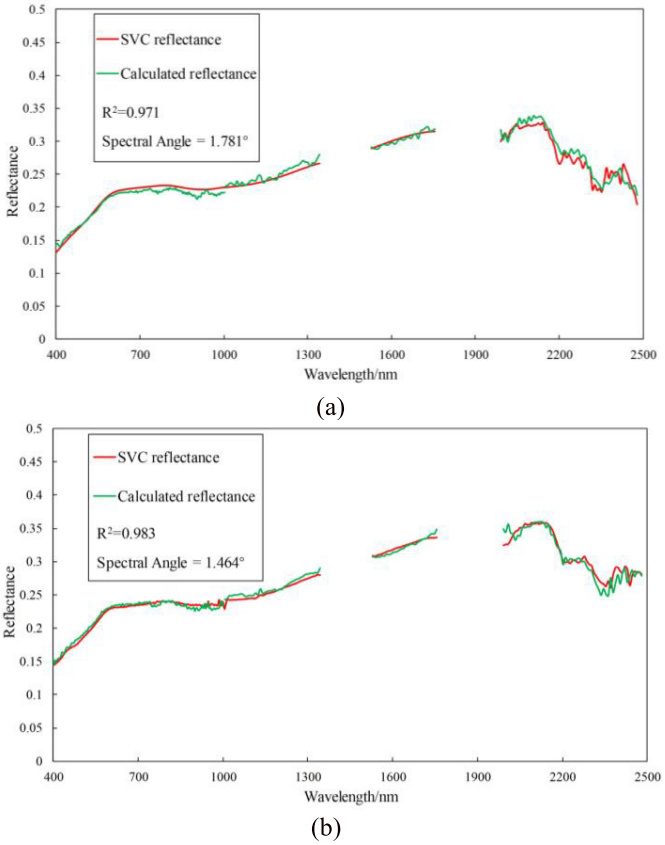

Fig. 7. Calibration accuracy on the Dunhuang validation data sets from 400 to 2500 nm. (a) Dunhuang, July 14, 2019. (b) Dunhuang, September 11, 2018.

of spectral angle which is less than 0.3 rad (17.2°) can be considered high degree of similarity [29].

Mathematically, a higher R^2 corresponds to a smaller root-mean-square error (RMSE), and a lower spectral angle represents a similar characteristic, indicating a better model performance.

Fig. 7 shows that the overall shape of the collected reflectance data on Dunhuang validation data sets has a high similarity with the reflectance-based results, as a function of the wavelength. The R^2 values are all greater than 0.95 and the spectral angle is all less than 2° between the measured reflectance and the results, which can be considered as a credible calibration. The calibration capability was then verified using two types of land cover from the different sites. In Table III, the wavelength was chosen corresponding to the Visual and Infrared Multispectral Imager (VIMI), which is the other optical imaging sensor load on GF-5. The standard deviation is calculated as follows:

$$\text{Std} = \frac{\sum_{i=1}^{N}(x_i - \bar{x})^2}{N} \tag{7}$$

where x_i denotes the data acquired from different periods on the chosen bandwidths. Std indicts the fluctuation on the same location and the same band during the similar but different imaging time.

The average reflectance ratio floats just a bit below 0.03 around the standard, which represents a good representation of the average reflectance of the calibrated results. Only the bands at about 1611 and 2201 nm show more than 2% variation between the collected reflectance data and the vicarious predictions. The uncertainty is higher in the SWIR range than in the VNIR range. The standard deviations of the ratios are less than 3% for each chosen band, which can be regarded as the level of repeatability in the calibration confidence determined in this work.

The radiometric calibration was carried out to obtain the reflectance data for each pixel of the image in a practical application. In this regard, for the cross-validation, the accuracy should be verified among two cover types, bare and grass. In this experiment, the ground reflectance data were collected using an Analytica Spectra Devices (ASD) FieldSpec portable spectrometer at the Xuzhou site. The measurement objectives were chosen as vegetation, which includes a number of biochemical responses in the spectrum, and bare soil. The spectrometer was used in a relative mode where we collected the data from a sunlit Spectralon reference panel and recorded ratio measurements of the different land-cover types with regard to those from the Spectralon panel. The Spectralon panel directional reflectance factor was calibrated in the laboratory before the field experiment. Figs. 8 and 9 show the comparison between the calibrated results and the reflectance data collected at the Xuzhou site for vegetation and bare soil. The ratios are around 1.0, indicating that the calibrated results are almost equal to the ASD measurement, except for the vegetation between 2000 and 2500 nm. The R^2 values are 0.947 and 0.981 for the bare soil and vegetation, respectively.

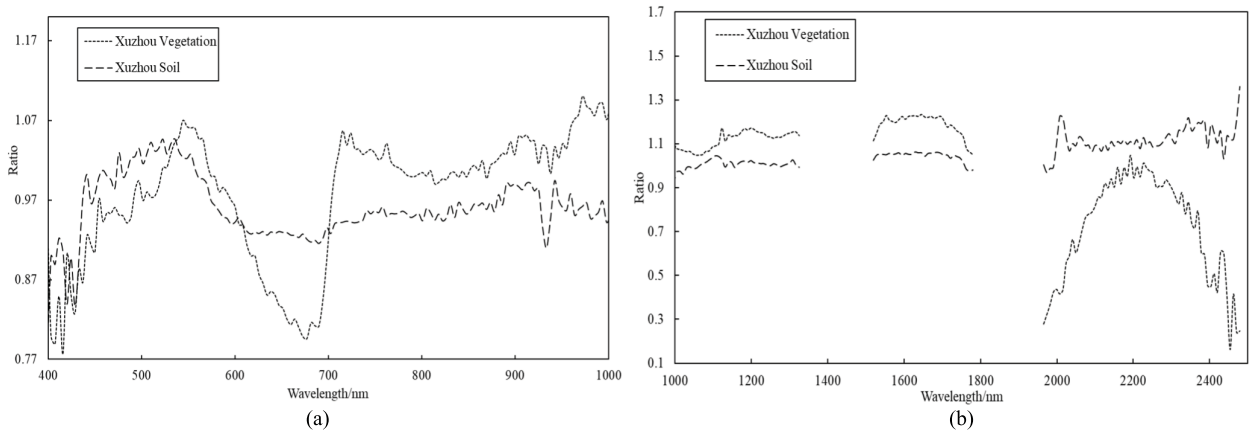

Fig. 8. Ratios of the ASD to AHSI surface reflectance for the calibration target at the Xuzhou site. (a) 400–1000 nm. (b) 1000–2500 nm.

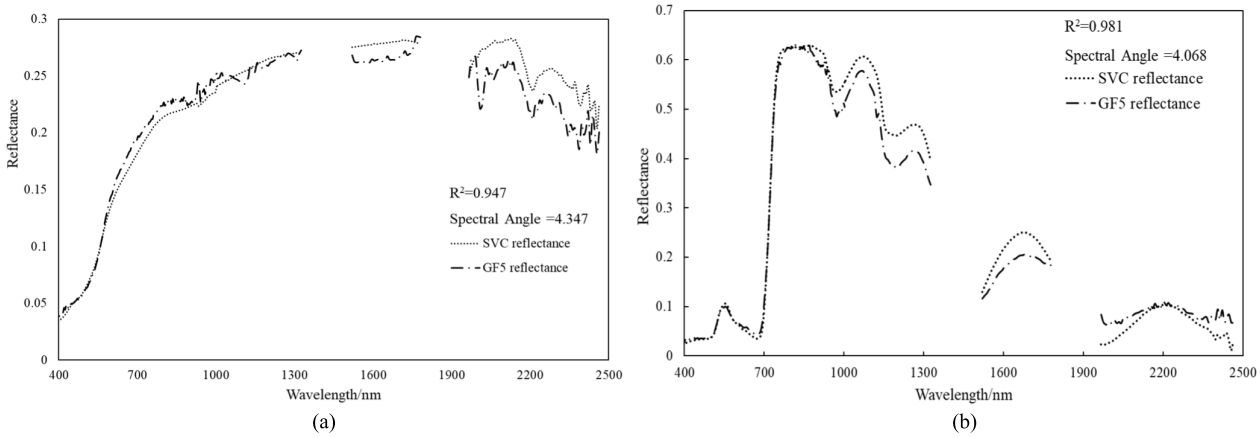

Fig. 9. Comparison of reflectance data for soil and vegetation at the Xuzhou site from 400 to 2500 nm. (a) Bare soil category. (b) Vegetation category.

TABLE IV
COMPARATION BETWEEN THE *In Situ* VALIDATION AND CROSS-VALIDATION

Validation (Acquisition time)	AHSI data	R^2	Spectral angle°
In situ (GF--5 transit time)	Dunhuang, 2019 Jul 14	0.971	1.781
	Dunhuang, 2018 Sep 11	0.983	1.464
	Xuzhou Bare soil, 2019 Jun 05	0.947	4.347
	Xuzhou Vegetation,2019 Jun 05	0.981	4.068
Landsat8, Dunhuang, 2019 Jul 19	Dunhuang, 2019 Jul 14	0.995	1.616
Landsat8, Dunhuang, 2018 Sep 08	Dunhuang, 2018 Sep 11	0.993	1.642
Landsat8, Xuzhou, 2019 Jun 06, Bare soil	Xuzhou Bare soil, 2019 Jun 05	0.969	10.148
Landsat8, Xuzhou, 2019 Jun 06, Vegetation	Xuzhou Vegetation, 2019 Jun 05	0.991	12.352
Sentinel2, Dunhuang, 2019 Jul 11	Dunhuang, 2019 Jul 14	0.990	1.511
Sentinel2, Dunhuang, 2018 Sep 09	Dunhuang, 2018 Sep 11	0.991	2.633
Sentinel2, Xuzhou, 2019 Jun 25, Bare soil	Xuzhou Bare soil, 2019 Jun 05	0.969	5.979
Sentinel2, Xuzhou, 2019 Jun 25, Vegetation	Xuzhou Vegetation, 2019 Jun 05	0.997	6.957

C. Comparation With Different Sensors

In this section, two complementary data sets from different multispectral cameras are included for the further performance assessment. The data sets for the two sites were provided by the Operational Land Imager and Sentinel-2 sensors. The coastal (443 nm), blue (483 nm), green (561 nm), red (655 nm), and NIR (865 nm) bands were considered for Operational Land Imager. The coastal aerosol (443 nm), blue (490 nm), green (560 nm), red (665 nm), vegetation red edge (705 nm), vegetation red edge (740 nm), NIR (842 nm), vegetation red edge (865 nm), water vapor (945 nm), SWIR cirrus (1.375 nm), SWIR (1.610 nm), and SWIR (2.190 nm) bands of Sentinel-2 were chosen for the near-coincident validation,

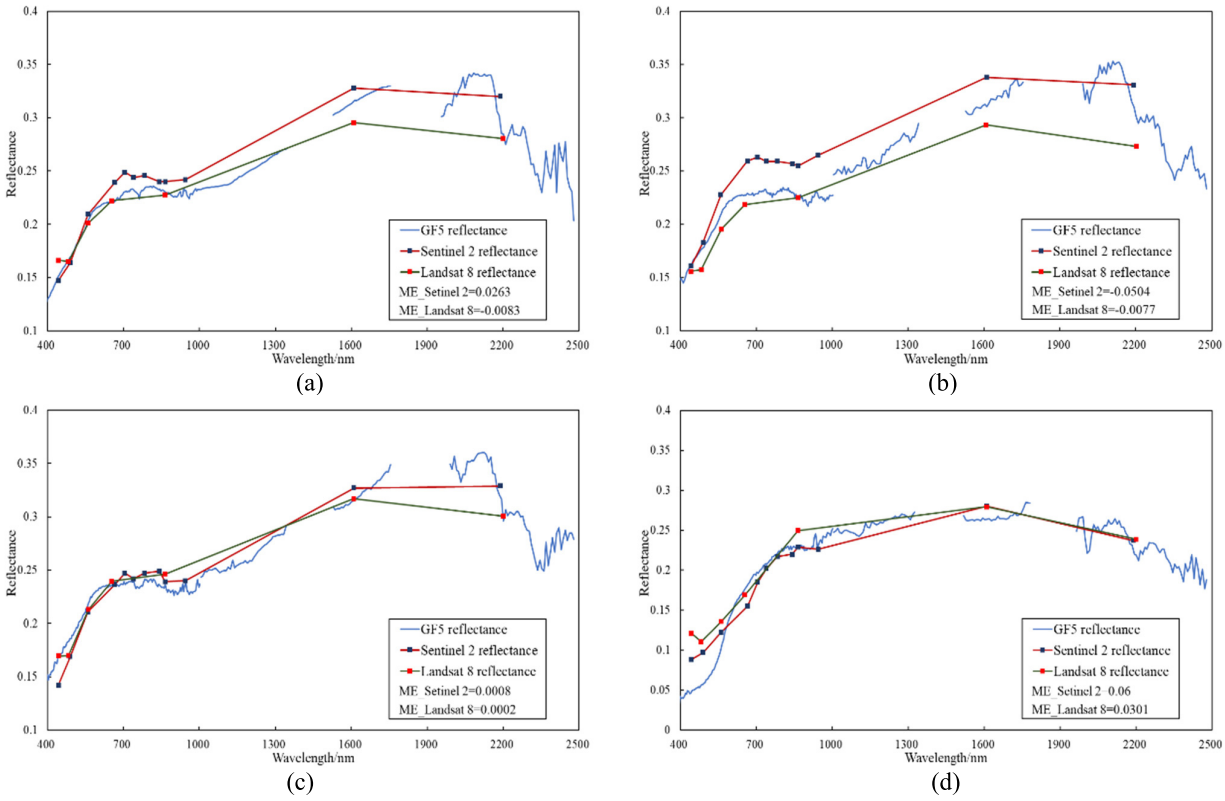

Fig. 10. Reflectance comparison at different sites. (a) Dunhuang site-September 10, 2019. (b) Dunhuang site-July 14, 2019. (c) Dunhuang site-September 11, 2018. (d) Xuzhou site-May 29, 2019.

and the reflectance values of the corresponding band center wavelengths in the AHSI instrument were interpolated. As shown in Fig. 10, the difference when compared with Landsat 8 at the Dunhuang site is under 0.01, which indicates that very little bias exists in the calibration results, compared with Landsat 8. When compared with these two sensors at the same wavelength, the calibrated reflectance of the AHSI instrument lies between that of Landsat 8 and Sentinel-2, and the mean difference is under 0.06. That is, the calibrated result of the AHSI instrument keeps a high consistency with the Landsat 8 and Sentinel 2. Table IV gives the comparation result between the *in situ* validation and cross validation and shows that R^2 values are all more than 0.94. R^2 values between different satellites imagery are greater than which of *in situ* surface reflectance, which proves a high consistency of AHSI and other two sensors. Because of the variation of the imaging time, the spectral angle of Xuzhou cross validation site is bigger than others.

V. Conclusion

In this study, surface reflectance data from the Dunhuang calibration site in China were utilized for the radiometric calibration of the AHSI instrument onboard the GF-5 satellite for the overpass on September 10, 2019. After this, an experiment was carried out at the Xuzhou site to verify the validity of the calibrated spectra using a spectral radiometer. From the coefficients obtained in this study, it can be concluded that the calibrated AHSI instrument showed a stable radiometric performance among two cover types, bare and grass. The ratio of surface reflectance to AHSI-derived surface reflectance was between 0.8 and 1.2 for all the bands, and was consistent with the reflectance data for the Dunhuang site. The R^2 values were all greater than 0.95 and the spectral angle is all less than 2°. The standard deviations of the ratios were less than 3% for each chosen band, which proved that the calibrated data had a high consistency with the *in situ* measurements. Moreover, the cross-validation at the Xuzhou site showed that the R^2 values were 0.947 and 0.981 for the bare soil and vegetation, respectively. The mean differences between the AHSI instrument and Landsat 8/Sentinel-2 were all under 0.06, which further demonstrated that the calibrated reflectance had a high accuracy. In this way, the calibration coefficients of all the bands were determined, which we recommend are utilized to make sure that the AHSI instrument meets the requirement of accurate radiometric characteristics.

Acknowledgment

The authors would like to thank the Shanghai Institute of Technical Physics, Chinese Academy of Sciences, Shanghai, China, for providing the Advanced Hyperspectral Imager (AHSI) data used in the experiments.

References

[1] Y. Sun *et al.*, "GF-5 satellite: Overview and application prospects," *Spacecraft Recovery Remote Sens.*, vol. 39, no. 3, pp. 1–13, 2018.
[2] Y.-N. Liu *et al.*, "The advanced hyperspectral imager: Aboard China's GaoFen-5 satellite," *IEEE Geosci. Remote Sens. Mag.*, vol. 7, no. 4, pp. 23–32, Dec. 2019.
[3] G. Chander and B. Markham, "Revised Landsat-5 TM radiometric calibration procedures and postcalibration dynamic ranges," *IEEE Trans. Geosci. Remote Sens.*, vol. 41, no. 11, pp. 2674–2677, Nov. 2003.

[4] F. D. van der Meer *et al.*, "Multi-and hyperspectral geologic remote sensing: A review," *Int. J. Appl. Earth Observ. Geoinf.*, vol. 14, no. 1, pp. 112–128, Feb. 2012.
[5] M. Roberts, "The role of atmospheric multiple scattering in the transmission of fluorescence light from extensive air showers," *J. Phys. G, Nucl. Part. Phys.*, vol. 31, no. 11, p. 1291, 2005.
[6] R. D. Schwartz, "Global dimming: Clear-sky atmospheric transmission from astronomical extinction measurements," *J. Geophys. Res., Atmos.*, vol. 110, no. D14210, pp. 1–6, Jul. 2005.
[7] B. Markham *et al.*, "Landsat-8 operational land imager radiometric calibration and stability," *Remote Sens.*, vol. 6, no. 12, pp. 12275–12308, Dec. 2014.
[8] P. M. Teillet, G. Fedosejevs, K. J. Thome, and J. L. Barker, "Impacts of spectral band difference effects on radiometric cross-calibration between satellite sensors in the solar-reflective spectral domain," *Remote Sens. Environ.*, vol. 110, no. 3, pp. 393–409, Oct. 2007.
[9] G. Chander, B. L. Markham, and J. A. Barsi, "Revised Landsat-5 thematic mapper radiometric calibration," *IEEE Geosci. Remote Sens. Lett.*, vol. 4, no. 3, pp. 490–494, Jul. 2007.
[10] H. McNairn *et al.*, "The soil moisture active passive validation experiment 2012 (SMAPVEX12): Prelaunch calibration and validation of the SMAP soil moisture algorithms," *IEEE Trans. Geosci. Remote Sens.*, vol. 53, no. 5, pp. 2784–2801, May 2015.
[11] G. T. Georgiev and J. J. Butler, "Long-term calibration monitoring of Spectralon diffusers BRDF in the air-ultraviolet," *Appl. Opt.*, vol. 46, no. 32, pp. 7892–7899, Nov. 2007.
[12] R. O. Green, B. E. Pavri, and T. G. Chrien, "On-orbit radiometric and spectral calibration characteristics of EO-1 hyperion derived with an underflight of aviris and *in situ* measurements at salar de arizaro, argentina," *IEEE Trans. Geosci. Remote Sens.*, vol. 41, no. 6, pp. 1194–1203, Jun. 2003.
[13] W. Frank Staylor, "Degradation rates of the AVHRR visible channel for the NOAA 6, 7, and 9 spacecraft," *J. Atmos. Ocean. Technol.*, vol. 7, no. 3, pp. 411–423, Jun. 1990.
[14] K. R. Castle *et al.*, "In-flight absolute radiometric calibration of the thematic mapper," *IEEE Trans. Geosci. Remote Sens.*, vol. GE-22, no. 3, pp. 251–255, May 1984.
[15] J. Barsi, J. Schott, S. Hook, N. Raqueno, B. Markham, and R. Radocinski, "Landsat-8 thermal infrared sensor (TIRS) vicarious radiometric calibration," *Remote Sens.*, vol. 6, no. 11, pp. 11607–11626, Nov. 2014.
[16] P. M. Teillet *et al.*, "A generalized approach to the vicarious calibration of multiple Earth observation sensors using hyperspectral data," *Remote Sens. Environ.*, vol. 77, no. 3, pp. 304–327, Sep. 2001.
[17] X. Hu *et al.*, "Characterization of CRCS dunhuang test site and vicarious calibration utilization for Fengyun (FY) series sensors," *Can. J. Remote Sens.*, vol. 36, no. 5, pp. 566–582, Oct. 2010.
[18] X. Xiong, W. Barnes, X. Xie, and V. Salomonson, "On-orbit performance of Aqua MODIS on-board calibrators," *Proc. SPIE*, vol. 5978, Oct. 2005, Art. no. 59780U.
[19] S. F. Biggar, K. J. Thome, and W. Wisniewski, "Vicarious radiometric calibration of EO-1 sensors by reference to high-reflectance ground targets," *IEEE Trans. Geosci. Remote Sens.*, vol. 41, no. 6, pp. 1174–1179, Jun. 2003.
[20] R. Frouin and C. Gautier, "Calibration of NOAA-7 AVHRR, GOES-5, and GOES-6 VISSR/VAS solar channels," *Remote Sens. Environ.*, vol. 22, no. 1, pp. 73–101, Jun. 1987.
[21] P. N. Slater *et al.*, "Reflectance- and radiance-based methods for the in-flight absolute calibration of multispectral sensors," *Remote Sens. Environ.*, vol. 22, no. 1, pp. 11–37, Jun. 1987.
[22] K. J. Thome, "Absolute radiometric calibration of Landsat 7 ETM+ using the reflectance-based method," *Remote Sens. Environ.*, vol. 78, nos. 1–2, pp. 27–38, Oct. 2001.
[23] K. Thome *et al.*, "ASTER preflight and inflight calibration and the validation of level 2 products," *IEEE Trans. Geosci. Remote Sens.*, vol. 36, no. 4, pp. 1161–1172, Jul. 1998.
[24] P. M. Teillet, "A framework for *in-situ* sensor measurement assimilation in remote sensing applications," in *Proc. 23rd Can. Symp. Remote Sens.*, Ste. Foy, Quebec, Aug. 2001, pp. 111–119.
[25] J. McCorkel, K. Thome, and L. Ong, "Vicarious calibration of EO-1 hyperion," *IEEE J. Sel. Topics Appl. Earth Observ. Remote Sens.*, vol. 6, no. 2, pp. 400–407, Apr. 2013.
[26] R. Kurucz, "The solar irradiance by computation," in *Proc. 17th Annu. Rev. Conf. Atmos. Transmiss. Models*, 1995, pp. 333–334.
[27] Z. Wang, "Ground test sites for absolute radiometric calibration of China resources satellite," *Remote Sens. Land Resour.*, vol. 41, no. 3, pp. 40–46, 1999.
[28] J. He and Y. Lu, "The measurement and evaluation of bidirectional reflectance characteristics of Dunhuang radiative calibration site," *J. Remote Sens.*, vol. 1, no. 4, pp. 246–251, 1997.
[29] K. Tan, C. Niu, X. Jia, D. Ou, Y. Chen, and S. Lei, "Complete and accurate data correction for seamless mosaicking of airborne hyperspectral images: A case study at a mining site in inner Mongolia, China," *ISPRS J. Photogramm. Remote Sens.*, vol. 165, pp. 1–15, Jul. 2020.

Kun Tan (Senior Member, IEEE) received the B.S. degree in information and computer science from Hunan Normal University, Changsha, China, in 2004, and the Ph.D. degree in photogrammetric and remote sensing from the China University of Mining and Technology, Xuzhou, China, in 2010.

From September 2008 to September 2009, he was a Joint Ph.D. Candidate of remote sensing with Columbia University, New York, NY, USA. From 2010 to 2018, he was with the Department of Surveying, Mapping, and Geoinformation, China University of Mining and Technology. He is currently a Professor with the Key Laboratory of Geographic Information Science (Ministry of Education), East China Normal University, Shanghai, China. His research interests include hyperspectral image classification and detection, spectral unmixing, quantitative inversion of land surface parameters, and urban remote sensing.

Xue Wang received the B.S. degree in geographic information system and the Ph.D. degree in photogrammetric and remote sensing from the China University of Mining and Technology, Xuzhou, China, in 2014 and 2019, respectively.

He is currently a Post-Doctoral Researcher with the Key Laboratory of Geographic Information Science (Ministry of Education), East China Normal University, Shanghai, China. His research interests include hyperspectral imagery processing, deep learning, and ecological monitoring.

Chao Niu received the B.S. degree in geographic information science and the M.S. degree in photogrammetric and remote sensing from the China University of Mining and Technology, Xuzhou, China, in 2017 and 2020, respectively. He is currently pursuing the Ph.D. degree in cartography and geographic information system with the Key Laboratory of Geographic Information Science (Ministry of Education), East China Normal University, Shanghai, China.

His research interests include hyperspectral image processing and quantitative inversion of water quality parameters.

Feng Wang (Member, IEEE) received the B.S. and M.S. degrees from Information Engineering University, Zhengzhou, China, in 2006 and 2010, respectively, and the Ph.D. degree from Fudan University, Shanghai, China, in 2017.

He was an Assistant Research Fellow with the Shanghai Institute of Technical Physics, Chinese Academy of Sciences, Shanghai. He is an Assistant Professor with the Key Laboratory for Information Science of Electromagnetic Waves (MoE), Fudan University. His research interests include radar imaging, hyperspectral remote sensing, and target recognition.

Peijun Du (Senior Member, IEEE) received the Ph.D. degree in geodesy and survey engineering from the China University of Mining and Technology, Xuzhou, China, in 2001.

He is a Professor of remote sensing and geographical information science with Nanjing University, Nanjing, China. He has authored more than 70 articles in international peer-reviewed journals and more than 100 articles in international conferences and Chinese journals. His research interests focus on remote sensing image processing and pattern recognition, hyperspectral remote sensing, and applications of geospatial information technologies.

Dr. Du is an Associate Editor of the IEEE GEOSCIENCE AND REMOTE SENSING LETTERS. He also served as the Co-Chair of the Technical Committee of URBAN2009, IAPR-PRRS 2012, EORSA 2014, IEOAs 2015, and CCGC 2015; the Co-Chair of the Local Organizing Committee of JURSE 2009, WHISPERS 2012, and EORSA 2012; and a member of the Scientific Committee or Technical Committee of other international conferences, including WHISPERS from 2010 to 2016, URBAN in 2011, 2013, and 2015, MultiTemp in 2011, 2013, and 2015, ISIDF in 2011, and the SPIE European Conference on Image and Signal Processing for Remote Sensing from 2012 to 2016.

De-Xin Sun received the B.S. degree from Shandong Normal University, Jinan, China, in 1996, and the M.S. and Ph.D. degrees from the Shanghai Institute of Technical Physics, Chinese Academy of Sciences (CAS), Shanghai, China, in 2000 and 2003, respectively.

Since 2005, he has been a Senior Researcher with the CAS Key Laboratory of Infrared Detection and Imaging Technology, Shanghai Institute of Technical Physics. His research interests include information acquisition and processing, design, and realization of optoelectronic systems.

Juan Yuan received the B.S. degree in geographic information system major from Shanxi Agricultural University, Jinzhong, China, in 2012, and the M.S. degree in forest economics major from Zhejiang A&F University, Hangzhou, China, in 2015.

From 2013 to 2015, she was jointly trained with the Center for Earth Observation and Digital Earth, Chinese Academy of Sciences, Beijing, China, studying spectral calibration of the hyperspectral imager. Since 2015, she has been an Intermediate Engineer with the Qidong Center of Photoelectric and Remote Sensing, Shanghai Institute of Technical Physics, Chinese Academy of Sciences, Shanghai, China. Her research interests include spectral calibration and radiometric calibration of the hyperspectral imagers, atmospheric radiometer development, and atmospheric correction.

Jing Zhang received the B.S. degree in optical information and technology major from Shanxi University, Taiyuan, China, in 2010, and the M.S. degree in optics from the Anhui Institute of Optics and Fine Mechanics, Chinese Academy of Sciences, Hefei, China, in 2013.

Since 2013, she has been an Assistant Researcher with the Shanghai Institute of Technical Physics, Chinese Academy of Sciences, Shanghai, China. Her research interests include remote sensing image processing, spectral calibration, and radiometric calibration of the hyperspectral imager.